An adjoint based forecast impact from assimilating MISR winds into the GEOS-5 data assimilation and forecasting system

Kevin J. Mueller[1], Junjie Liu[1], Will McCarty[2], and Ron Gelaro[2]

[1] Jet Propulsion Laboratory, California Institute of Technology; [2] Goddard Space Flight Center (GSFC)

Corresponding author: Junjie Liu Junjie.Liu@jpl.nasa.gov

1 Abstract

2 This study examines the benefit of assimilating cloud motion vector (CMV) wind

3 observations obtained from the Multi-angle Imaging SpectroRadiometer (MISR)

4 within a Modern-Era Retrospective Analysis for Research and Applications-2

5 (MERRA2) configuration of the Goddard Earth Observing System-5 (GEOS-5) model

6 Data Assimilation System (DAS). Available in near real time (NRT) and with a

7 record dating back to 1999, MISR CMVs boast pole-to-pole coverage and geometric

8 height assignment that is complementary to the suite of Atmospheric Motion

9 Vectors (AMVs) included in the MERRA2 standard. Experiments spanning

10 September-October-November of 2014 and March-April-May of 2015 estimated

11 relative MISR CMV impact on the 24-hour forecast error reduction with an adjoint

12 based forecast sensitivity method. MISR CMV were more consistently beneficial and

13 provided twice as large a mean forecast benefit when larger uncertainties were

14 assigned to the less accurate component of the CMV oriented along the MISR

15 satellite ground track, as opposed to when equal uncertainties were assigned to the

16 eastward and northward components as in previous studies. Assimilating only the

17 cross-track component provided 60% of the benefit of both components. When

18 optimally assimilated, MISR CMV proved broadly beneficial throughout the Earth,

19 with greatest benefit evident at high latitudes where there is a confluence of more

20 frequent CMV coverage and gaps in coverage from other MERRA2 wind

21   observations. Globally, MISR represented 1.6% of the total forecast benefit, whereas

22   regionally that percentage was as large as 3.7%.

1 Introduction

2   Atmospheric motion vectors (AMVs), a proxy measure of wind, are

3   indispensable to regional and global numerical weather prediction (NWP) models

4   and analyses. Derived from tracking cloud or water vapor features in satellite

5   imagery, AMVs fill some critical conventional observation data gaps (e.g., the Arctic,

6   Antarctic and global oceans). However, there remain regions where wind

7   observations are sparse or unavailable, notably in the high latitude band (55-65°

8   North/South) between AMVs obtained from regular geosynchronous (GEO)

9   instrument imagery and those obtained from consecutive orbits of lower earth orbit

10 (LEO) instruments. AMVs from composite LEO-GEO (e.g. Lazzara et al., 2014) and

11 from constellations of LEO instruments (e.g. Borde et al., 2016) increasingly, but not

12 entirely, mitigate these gaps. AMVs from LEO are also limited at low levels

13 (pressures > 700 hPa) by concerns about the accuracy of the radiometric heights

14 assigned there, which have led multiple NWP centers to exclude low level AMVs

15 from operational assimilation (Salonen et al., 2015). Cloud motion vector wind

16 observations derived from the Multi-angle Imaging SpectroRadiometer (MISR)

17 instrument onboard the polar-orbiting Terra could help mitigate the above coverage

18 gaps (Mueller et al., 2013), since their heights are retrieved by geometric techniques

19 and their coverage is nearly global and concentrated in the lower troposphere.

20

21   MISR measures reflected solar radiation in four bands from onboard the sun-

22   synchronous Terra satellite at nine distinct viewing zenith angles including nadir

23   (0°) and four angles (26°, 46°, 60°, and 70°) distributed along-track both forward

24   and aft relative to Terra's flight direction. The motion and height of underlying

25   cloud features are obtained from a single MISR overpass by tracking their

26   progression within 275 m resolution 380 km swath width red band imagery over

27   the 3.5 minute interval between the initial 70° forward view and nadir, and then

28   again for the same interval between nadir and the final 70° aft view (Horvath and

29   Davies, 2001a; Mueller et al., 2013). Aside from the nadir and 70°, a third view

30   angle of 26° is necessarily used to differentiate between parallax and along-track

31   cloud motion. This approach yields a precise geometric height and cross-track wind

32   component, but a relatively less precise along-track wind that is sensitive to the

33   accuracy of feature tracking and georegistration (Zong et al, 2002; Horvath and

34   Davies, 2001). The MISR wind height, cross-track, and along-track components have

35   respective precision of 190 m, 1.1 ms^{-1}, and 1.8 ms^{-1} (Horvath 2013). The retrieval

36   algorithm is attuned to stratocumulus, frequently tracking them despite the presence

37   of overlying clouds with less distinct texture. As a result, the overwhelming

38   majority (>95%) of MISR CMV sampling is found at low levels, and sampling is far

39   better over ocean than land.

40   The geometric heights assigned to MISR CMVs are not prone to the significant

41   difficulties with radiometric heights assigned to other AMVs, which are recognized

42   as a key limitation to their forecast benefit (Su et al., 2012). AMV height uncertainty

43   accounts for 70% of vector wind differences between other types of AMV and

5

44 rawinsonde (Velden et al., 2008). Particularly uncertain are low level radiometric

45 heights (pressures >700 hPa) assigned to broken or semitransparent clouds or in

46 regions where the temperature lapse rate is small (e.g., polar regions) or inverted

47 (e.g., the marine boundary layer). In the arctic, where these conditions are typical,

48 low level AMVs are deemed unreliable (Key et al., 2003; Santek et al., 2010). In

49 comparisons with AMVs derived from the Geostationary Operational Environmental

50 Satellite (GOES), MISR CMVs have been shown to have less biased heights in the 800

51 hPa – 600 hPa (~2-4 km height) range (Mueller et al., 2017), consistent with similar

52 findings of AMV height bias relative to reanalysis (Salonen et al., 2015). At the same

53 time, MISR CMV heights are prone to uncertainty distinguishing parallax from along-

54 track motion, leading to correlation of error in these components and tendency to

55 overestimate the heights of upper level (> 300 hPa (~7 km)) CMVs, though these

56 comprise less than 5% of total CMV sampling (Mueller et al., 2017).

57   Several studies have provided preliminary evaluations of the forecast benefit

58 MISR winds might provide. The first of these studies, Baker et al., 2014, employed

59 an adjoint method to quantify the reduction of 24-hour forecast errors from

60 assimilating MISR CMV amongst a suite of additional observations with the NAVy

61 Global Environmental Model (NAVGEM) 4D-Var Data Assimilation System. They

62 found that MISR winds reduced 24-hour global forecast errors, attributing much of

63 that error reduction to lessening a relative dearth of low-level wind observations

64 assimilated by their model. Yamashita (2014) tested assimilation of MISR CMV in

65 addition to routine observations within the 4D-VAR NWP system of the Japan

66 Meteorological Agency, and found increased forecast skill over all. Cress et al., 2014,

67   assimilated MISR CMV within the operational 3D-VAR numerical weather prediction

68   (NWP) system of the German Weather Service for summer and winter of 2010,

69   finding a benefit to the anomaly correlation of 500 hPa geopotential heights

70   between forecast and analysis.

71   These previous studies directly assimilated zonal and meridional components

72   of MISR CMV retrievals, with no explicit mechanism to capitalize on the greater

73   accuracy of the cross-track components of winds reported by MISR. In this study, we

74   have decomposed MISR CMV into along-track and cross-track in order to assign

75   appropriate uncertainties to each component and also explored the impact of

76   assimilating only the more accurate cross-track component. Complementing earlier

77   studies, we evaluate the forecast impact of MISR CMV using the Modern-Era

78   Retrospective Analysis for Research and Applications-2 (MERRA2) 3D-VAR

79   configuration of the Goddard Earth Observing System-5 (GEOS-5) model Data

80   Assimilation System (DAS) (Gelaro et al., 2017).

81   The remaining sections are organized as follows: section 2 describes the

82   datasets, experiments and diagnostic tools used to assess MISR winds benefit to the

83   analysis and forecast. Section 3 summarizes the results, including comparison of

84   techniques and parameters for assimilating MISR winds. Section 4 provides

85   discussion and conclusions.

2 Data and methods

2.1 Review and use of MISR CMV products

Two distinct sources of MISR CMVs are employed in this study, the monthly aggregated MISR Level 3 CMV product and the Level 2 NRT CMV product. The two products are available online and respectively tagged as MI3MCMVN and MI2TC_CMV_HDF_NRT at the NASA Langley Distributed Active Archive Center. The former is available with 24 hour latency archived back to 2000, the latter with NRT latency (95% of CMVS in under 2.5 hours) archived 30 days back from present. Excluded from this study are two other MISR products containing CMV less suitable for assimilation. The MISR Level 2 Cloud product (tagged MIL2TCSP) contains a superset of CMV from the Level 3 CMV product that includes retrievals of lower quality. The MISR Level 2 Stereo product (tagged MIL2TCST) contains less accurate CMV retrieved by a legacy algorithm.

The Level 2 NRT CMV product uses the same retrieval and quality control algorithms as the standard Level 3 CMV product, generating results comparable to the latter. However, the two products have minor differences owing to differences between the NRT and standard processing (STD) versions of upstream Level 0 (L0) and Level 1 (L1) data inputs. The NRT software pipeline is applied to incoming L0 instrument and satellite data in sessions associated with as little as five minutes of data, whereas the standard pipeline operates on the same data consolidated into sessions comprising one full orbit (90 minutes). Without this consolidation, NRT

8

108 processing is subject to lost coverage associated with gaps in the availability of

109 necessary inputs at time of processing.   Additionally, the continuously updated

110 record of corrections to camera pointing used to perform in-flight geometric

111 calibration is sensitive to the differences between NRT and STD processing.

112 Calibration discrepancies are responsible for a root-mean-square-vector-difference

113 (RMSVD) of 3 m s^{-1} between collocated Level 2 NRT CMVs and Level 3 CMVs

114 (Mueller et al., 2013b).

115

116 **2.2   GEOS-5 model, assimilation system, and adjoint methodology**

117   This study employs version 5.13.0 of the GEOS-5 DAS, with revisions to support

118 MISR winds assimilation and determination of adjoint sensitivity. Version 5.13.0 is

119 associated with officially released GEOS-5 data products between 20 September

120 2014 and 1 May 2015. The C180 (1/2 degree latitude-longitude) grid with 72 layers

121 between the surface and 0.01 hPa is employed, with default version 5.13.0 model

122 parameters and assimilated observations (other than MISR CMV) defined by the

123 MERRA-2 reanalysis (Gelaro et al., 2017). MERRA-2 incorporates a broad range of

124 observations, including geostationary AMVs from GOES,

125   The meteorological analysis in GEOS-5 uses the Gridpoint Statistical

126 Interpolation (GSI) 3D-Var [Wu et al., 2002; Purser et al., 2003a, 2003b] assimilation

127 methods. The objective of the assimilation is to produce an analysis field for which a

128 cost function constructed from the observation-minus-analysis (O-A) residuals is

129 minimized subject to assumed forecast and observation error statistics [Cohn,

130 1997]. The GSI performs minimization relative to control variables including stream

131 function contribution from wind, unbalanced velocity potential function, unbalanced

132 temperature, unbalanced surface pressure, moisture, cloud water, ozone, and

133 coefficients for the bias correction of the satellite radiance data.

134   An adjoint sensitivity method is employed to calculate the impact of each

135 individual observation on the short-range forecast simultaneously, producing

136 results that can be easily aggregated by data type, location, channel, etc [Gelaro et

137 al., 2007; Zhu and Gelaro, 2008; Gelaro et al., 2010]. It is the same method used

138 operationally to monitor and evaluate the impact of assimilated observations.

139 Impacts are measured relative to 24-hour and 30-hour forecast error differences in

140 total moist energy. The forecast error is measured against analysis state at the

141 verification time, t=24 hours (Langland and Baker, 2004). The 24-hour and 30-hour

142 forecast are initiated at time, t=0 hours, and at time, t=-6 hours, respectively. The

143 difference between the former and latter forecasts are due to observations

144 assimilated at the analysis time t=0 hours. The method is undertaken for every 6-

145 hour time step, facilitating impact assessment of all assimilated observations in each

146 experiment.

147

148 **2.3   Experiments**

149 **2.3.1   Thinning and screening methods**

150   MISR CMV are reported with 17.6 × 17.6 gridded resolution with vertical

151 coordinates of height relative to the Earth's ellipsoid. For this study, the set of CMV

152 reported per time step was thinned such that only one CMV could be assimilated per

153 100 km x 100 km x 100 hPa volume on a model aligned grid. This thinning included

154 simple transformation of MISR reported geometric height, *h*, into pressure

155 coordinates assuming a constant standard atmosphere, that is:

$$p = p_s e^{-kh}$$

156 where k=1.186×10^{-4} m^{-1}, and p_s=1013.25 hPa. Note that this height-pressure

157 conversion formula was only used in the thinning process, while the model

158 geometric height and observation height was used in vertical interpolation during

159 data assimilation process. In addition to spatial thinning, MISR CMV with heights

160 reported below model surface elevation or above 15 km were also excluded. For all

161 the experiments listed in section 2.3.3, a gross-error threshold was also applied to

162 screen CMV differing from background state by more than 8.0 ms^{-1}.

163   Quality Indicator (QI) values assigned to MISR CMV were given no influence on

164 the uncertainty assigned during assimilation. CMV QI values are a measure of

165 retrieval consistency between neighbors and between redundant forward and aft

166 camera based estimates. German Weather Service experiments found CMV QI to

167 poorly predict CMV influence on forecast skill (Cress, 2014). Consistent with their

168 finding, our own experiments show negligible correlation between per observation

169 MISR CMV forecast impact and QI.

170

171 **2.3.2   Assimilation methods, uncertainty assignment, and assimilation experiments**

172   Table 1 lists model experiments, three of which differ in the way the winds were

173 assimilated and the uncertainty was assigned to each MISR CMV, all sharing the

174 same September-October-November (SON) time period in 2014.   In the first

175   experiment, labeled UV,, we assimilate MISR zonal (u) and meridional wind (v)

176   directly, the same as the assimilation methods employed in previous MISR wind

177   assimilation studies (e.g., Baker et al., 2014). The uncertainties applied with this

178   method are 3.0 ms^{-1} for the u and v vector components. The components are not

179   treated independently, so either both components are rejected or neither during

180   assimilation. In the second experiment, labeled ATCT, each MISR CMV is translated

181   into along-track and cross-track components based on viewing geometry that are

182   then assimilated independently with respective uncertainties of 8.0 ms^{-1} and 2.0 ms^{-}

183   ^{1}. This approach takes advantage of the cross-track having greater theoretical

184   accuracy (Zong et al, 2002; Horvath and Davies, 2001). The assigned uncertainty for

185   the cross-track wind is the same as assessed in validation studies (Horvath 2013,

186   Mueller et al., 2017). The uncertainty of 8.0 m/s for the along-track MISR CMV is

187   conservative, being set much greater than the global along-track RMS difference

188   relative to GOES AMV (3.2 ms^{-1}) in order to limit the potential influence of along-

189   track bias and regions of greater uncertainty (Mueller et al., 2017). In the third

190   experiment, labeled CT, only the more accurate cross-track wind component is

191   assimilated. Lastly, a control experiment, labeled CONTROL, was conducted for the

192   same time period, but with no assimilation of MISR CMV.

193   In addition to the above experiments comparing assimilation methodology, two

194   variations of the ATCT experiment were conducted using the same assimilation

195   approach. The first, labeled NRT, uses the MISR NRT CMV product rather than the

196   MISR L3 CMV product, to compare their relative effectiveness. The second, labeled

197   ATCT15 extends the timespan of our analysis to March-April-May (MAM) of 2015.

3 Results and Discussion

3.1 Overview

In the following sections, we investigate the performance of three assimilation approaches through comparisons among the CT, UV, and ATCT experiments (3.2); compare the sampling and net impact of MISR CMV relative to other assimilated observations for the ATCT and ATCT_15 experiments (3.3); and assess the consistency of MISR CMV sampling and forecast impact between the NRT CMV and the standard processing (3.4).

3.2 Sensitivity of forecast impact to three methods of assimilating MISR CMVs

Comparisons of mean forecast benefit among ATCT, UV, and CT experiments applying distinct assimilation methodologies to the same data inputs demonstrate the superiority of the ATCT approach. As shown in Table 2, the mean impact per six-hour time step contributed by the assimilated MISR CMV was -25 ± 18 mJ kg^{-1} for ATCT, roughly twice that of UV and 70% greater than that of the CT experiment.

Figures 1d, e, and f present observation-minus-forecast (OMF) (six-hour forecast) statistics, showcasing negligible OMF bias for assimilated cross-track components of MISR CMV during the ATCT experiment, but bias as large as 2.0 m s^{-1} for the along-track component. In the absence of model or observation bias, OMF should be unbiased (e.g., Kalnay 2003). Here, along-track OMF bias follows a pattern broadly consistent with that seen in comparison between MISR CMVs and GOES AMVs (Mueller et al., 2017). The along-track component bias at lower levels (below 750 hPa) is proportional to height. The bias changes from negative to

220   positive around the peak height of sampling density, at 850 hPa in the top row of

221   Figure 1. This is a consequence of the correlation (Zong et al., 2002) between error

222   in the height and error in the along-track component of MISR CMVs causing

223   preferential sampling of negative/positive along-track bias at heights below/above

224   the peak in sampling. Above 750 hPa, MISR CMV along-track bias has no such

225   gradient, instead being consistently on the order of 1-2 ms^{-1} at high latitudes where

226   the majority of sampling is found. Over the tropics, where sampling is sparse, the

227   bias is not evident. Figures 1d, 1e, and 1f also show bias profiles for the UV

228   experiment, wherein the same underlying positive along-track bias manifests as

229   principally southward component bias at low latitudes and both westward and

230   southward bias at mid to high latitudes.

231   Evident in Figures 1g, h, and j, heights and regions where the along-track bias is

232   most pronounced in the ATCT experiment also show the largest discrepancies

233   between UV and ATCT in the forecast error reduction. This is most evident in the

234   southern extra-tropics where assimilation of the v component in the UV experiment

235   actually degrades the forecast for mid-level CMVs at heights from 900 hPa to 500

236   hPa. In contrast, the along-track component in the ATCT experiment is consistently

237   beneficial. In contrast to the v component, the assimilated u component consistently

238   improves the forecast, but to a far lesser degree than the assimilated cross-track

239   component in the ATCT experiment, which is largely due to the large u component

240   bias (Figure1 d, e, and f) and random errors relative to cross-track component (2.5

241   m/s vs. 2.1 m/s). It is also evident in Figures 1a, 1b, and 1c that the same heights

242   and regions where the v-component degraded the UV forecast also produced a

14

243   greater number of rejected CMV in UV relative to ATCT. The northern extra-tropics

244   exhibit the same trends as above, though to a lesser extent. The trends observed in

245   the tropics represent an instructive counterpoint. Because the mean along-track

246   bias is less consistent and not as large there, and because the projection of cross-

247   track and along-track winds is more aligned with u and v components there, the

248   forecast benefit is roughly equivalent for the ATCT and UV experiments.

249   For the CT experiment, the along-track component was excluded all together.

250   As evident for all latitude bands (Figures 1g, h, and i), assimilating CT only

251   consistently reduced the forecast error, but choosing not to assimilate the along-

252   track component had an adverse effect on the benefit provided by the cross-track

253   component, especially over the extra-tropics, reducing its benefit by as much as

254   40%. Riishojgard et al. (2008) also showed that single wind component

255   assimilation produced a poorer representation of that field in the analysis state.

256   They argued that the analysis accuracy of single wind assimilation depends more on

257   the forecast error covariance specified in data assimilation compared to assimilating

258   two wind components. Stoffelen et al. (2005) and Marseille et al. (2008) also argued

259   that proper background error covariance is essential to maximize single wind

260   observation impact. In CT, we used the same forecast error covariance as in the

261   ATCT case. The poorer performance of CT indicates that the default forecast error

262   covariance does not accurately capture the relationships between different

263   dynamical variables. Since the wind and mass fields, such as pressure, are more

264   tightly coupled over the extra-tropics in the forecast error covariance, the

265   degradation of assimilating a single component is larger over the extra-tropics

266   compared to the tropics (Figure 1g, h, and i).

267   **3.3   MISR forecast impact relative to other instruments**

268   The global 24-hour forecast impact amongst MISR CMVs and other classes of

269   satellite instruments is compared for the ATCT_15 experiment in Figure 2a. (The

270   results of the comparable ATCT experiment are roughly equivalent, with minor

271   differences discussed in section 3.4). MISR CMVs represent 1.6% of the total

272   forecast benefit from all of the observations, while AMVs from lower earth orbit

273   (LEO) and geosynchronous (GEO) represent ~15%. The total impact of satellite

274   winds is second behind that of infrared (IR) and microwave (MW) radiance

275   observations, which represent just over 50%. Rawinsonde and dropsonde profiles

276   (labeled RAOB+SND) and in-situ aircraft measurements that include wind,

277   temperature, and pressure each represent another ~12%. Surface wind forcing as

278   measured by microwave scatterometers represent 1% of impact. An additional

279   10% of forecast impact not plotted in Figure 2a is contributed by various land- and

280   ship-based observations, by radio occultation observations, and by pilot-balloon

281   measurements of wind. Figure 2b shows the per-obs impact of MISR CMV to be the

282   largest of the above observation groups, with magnitude comparable to RAOB+SND.

283   MISR CMVs are broadly beneficial everywhere, with greatest benefit evident at

284   high latitudes where there is a confluence of more frequent CMV coverage and gaps

285   in coverage from other wind observations. For example, Figure 2c shows that MISR

286   CMV contributes 3.7% of the total forecast benefit between latitudes 55° and 70°

287   South, more than double that of the global mean forecast impact of 1.6%. Figure 3

16

288   shows coverage for classes of wind observations, where coverage is defined by the

289   fraction of 6 hour periods during which one or more observation was assimilated

290   within each 2.5° latitude × 2.5° longitude grid cell. Figure 3a shows the frequency of

291   CMV coverage in the months of SON to be under 10% at low latitudes, and up to

292   20% or 50% depending on season at high latitudes. MISR CMV coverage is

293   primarily governed by the satellite repeat interval, varying from 9 days at the

294   equator to as little as 90 minutes near the poles, and by seasonal variation of

295   available sunlight at high latitudes. Greater MISR CMV sampling at high latitudes

296   synergistically coincides with gaps between LEO and GEO AMV coverage evident in

297   Figure 3b, ultimately producing greater forecast benefit for those regions as evident

298   in Figure 4a. Over the Southern Ocean, these regions also coincide with a paucity of

299   aircraft and sonde observations (Figures 3d & 3e), and, correspondingly, even

300   greater forecast benefit. Another region of enhanced MISR CMV benefit (Figure 4a)

301   is found over central Asia in the gap between GEO AMVs captured from Meteosat-9

302   and MTSAT-2 instruments (Figure 3b). The region also lacks frequent coverage

303   from aircraft and sondes (Figures 3e & 3f), to the extent that the rare instances of

304   MISR CMV retrieved there have outsized influence. Over ocean, the geographic

305   distribution of forecast benefit from MISR CMVs is rather similar to that of

306   scatterometer winds, possibly reflecting the fact that both largely or entirely

307   provide low level constraints on the wind field (Figures 3c and 4c). For example,

308   both provide negligible benefit over large swaths of the tropical Pacific and Atlantic

309   oceans, which is primarily due to the dense wind observations from the default LEO

310   and GEO satellites (Figure 4b). Although the forecast benefit from MISR CMV is

311 evidently enhanced where coverage from other wind observations is sparse, MISR

312 CMVs also exhibit significant benefits in well-sampled regions such as the North

313 Pacific.

3.4 Sensitivity of MISR wind forecast impact to assimilation time period and

315 **MISR CMV products**

316 ATCT_15 and ATCT were carried out over two different seasons: boreal summer

317 and fall respectively. Comparing these two experiments helps identify the sensitivity

318 of MISR wind impact to time of year, while aggregating them provides six months of

319 simulation. On a daily basis, MISR CMVs provide a consistent 24-hour forecast

320 benefit throughout ATCT and ATCT_15 as indicated in Figure 5 by a time series of

321 per orbit forecast impact wherein the running mean over 15 orbits (i.e. the rough

322 equivalent of 24 hours) is always beneficial (i.e. negative contribution to forecast

323 error norm). Measurements of forecast impact are inherently noisy, with the

324 standard deviation of per orbit CMV impact having comparable magnitude to the

325 mean, that is 10 J kg^{-1} ×10^{-3}. Still, the overwhelming majority (88%) of orbits with

326 MISR CMV sampling are found to provide a net forecast benefit, while the infrequent

327 remainder is broadly distributed, such that no duration of sequential orbits

328 contributes a significant regression. The largest single orbit forecast regression is

329 28.9 J kg^{-1} ×10^{-3} during ATCT. As visualized in Figure 5 and Table 2, the number of

330 MISR CMV assimilated on a per-orbit basis (2500) varies little (±360) in ATCT or

331 ATCT_15. Nor does the number of CMV rejected (330±110) during computation of

332 model analysis state through incremental minimization of the GSI cost function.

333

334   The near equivalence of CMV six-hourly forecast impacts in ATCT and ATCT_15

335   is a coincidental byproduct of ATCT producing 16% greater impact per orbit offset

336   by 25% fewer orbits producing valid CMV sampling.   The greater per-orbit CMV

337   benefit in ATCT can be traced to seasonality of sampling, with ATCT having a greater

338   fraction of total sampling located over the Southern Ocean where the model most

339   benefits from assimilating CMVs. The sampling deficit in ATCT can be traced to two

340   gaps evident in Figure 5 that were caused by a temporary suboptimal software

341   configuration affecting Terra attitude data that had been used in the MISR standard

342   processing chain during September 2014. The underlying issue, which was

343   identified and rectified in November 2014, did not affect other Terra instruments or

344   MISR science products, and also did not affect MISR NRT processing- hence the

345   absence of gaps in Figure 6 corresponding to those evident in Figure 5.

346

347   Figure 6 shows time series of the MISR CMVs impact and observation count in

348   the NRT experiment, which assimilates MISR NRT CMVs. Relative to standard

349   processing, the NRT CMVs are prone to losses of sampling due to timeliness of

350   necessary data input. As a result, NRT assimilates less samples per orbit (1900)

351   with greater variability of per orbit sampling (±600). Relative to ATCT, the fraction

352   of sampling in NRT (76%) is consistent with the fraction of forecast benefit (72%)-

353   that is 6.8 out of 9.5 J kg^{-1} ×10^{-3}. The distribution and magnitude of forecast

354   regressions on a per orbit basis are also comparable to ATCT.

355

19

4 Conclusions

A series of experiments have been conducted, demonstrating the benefit of assimilating cloud motion vectors from the MISR CMVs over periods covering September-October-November of 2014 and March-April-May within the GEOS-5 DAS as determined by an adjoint based forecast sensitivity method. Whereas previous studies have directly assimilated the zonal and meridional components of MISR CMVs, this study demonstrates more consistently beneficial and twice as large a mean forecast benefit when assimilating along-track and cross-track components and assigning larger uncertainties to less accurate along-track component. Although the more certain cross-track component contributes more than 90% of the total forecast benefit when assimilating both along-track and cross-track, assimilating only the latter provides only 60% of the forecast benefit as both. Systematic along-track bias in MISR CMVs consistent with earlier studies was evident in OMF statistics. This factored into the benefits of assigning greater uncertainty to the along-track. Another approach worth investigating would be application of a height- and possibly latitude- dependent along-track bias correction.

The overall benefit of optimally assimilating MISR CMVs was a 1.6% contribution to the global reduction of the moist energy error norm for 24-hour forecasts, with about twice that percentage of contribution in regions such as the Southern Ocean that are less well observed. Note that the impact on 24-hour forecast error reduction is only one measure of the observation impact. The overall reduction on 24-hour forecast errors from assimilating MISR winds corroborates

378 earlier studies showing an overall benefit from MISR CMVs as measured by various

379 metrics within multiple models (e.g., Yamashita (2014)). The magnitude of benefit

380 is promising in regard to the multi-angle retrieval of CMVs, given the limitations on

381 MISR coverage imposed by its relatively narrow 360 km swath. A single wider-

382 swath multi-angle imager, a tandem convoy of such imagers (which avoids the

383 ambiguity between parallax and along-track motion), or a multitude of low cost

384 nano-satellite variants could all provide significantly greater forecast benefit.

5 ACKNOWLEDGMENTS

6   REFERENCES

Baker, N. L., P. M. Pauley, R. H. Langland, K. Mueller, and D. Wu, 2014: An assessment of the impact of the assimilation of NASA TERRA MISR atmospheric motion vectors on the NRL global atmospheric prediction system. *Second Symposium on the Joint Center for Satellite Data Assimilation, 94th American Meteorological Society Annual Meeting. Atlanta, Georgia, Georgia World Congress Center.* http://www.jcsda.noaa.gov/documents/meetings/AMS2014/2nd_JCSDA_Baker_ MISR.pptx

Borde, R., O. Hautecoeur, and M. Carranza. (2016) EUMETSAT Global AVHRR Wind Product. *J. Atmos. Ocean. Tech.*, **133**, 429-438

Cohn, S. E., 1997: An introduction to estimation theory. J. Meteor. Soc. Japan, 75, 257-288

Cress, A., (2014) Improving the Use of Satellite Winds at the German Weather Service, (2014) *Twelfth International Winds Workshop*, Copenhagen, Denmark. http://www.eumetsat.int/website/wcm/idc/idcplg?IdcService=GET_FILE&dDo cName=PDF_CONF_P61_S4_02_CRESS_V&RevisionSelectionMethod=LatestRele ased&Rendition=Web

Gelaro, R., Y. Zhu, and R. M. Errico, 2007: Examination of various-order adjoint-based approximations of observation impact. *Meteorologische Zeitschrift* **16**, 685–692.

Gelaro R, R. H. Langland, S., Pellerin, and R. Todling, 2010: The THORPEX observation impact inter-comparison experiment. *Mon. Weather Rev.* **138**: 4009– 4025.

23   Gelaro, R., and Coauthors, 2017: The Modern-Era Retrospective Analysis for Research

24   and Applications, version 2 (MERRA-2). *J. Climate*, **30**, 5419–5454

25   Horvath, Á. and R. Davies, 2001: Feasibility and error analysis of cloud motion wind

26   extraction from near-simultaneous multiangle MISR measurements, Journal of

27   Atmospheric and Oceanic Technology, 18-4, 591-608

28   Horváth, Á. 2013: Improvements to MISR stereo motion vectors., *J. Geophys. Res*., 118

29   Kalnay, E. (2003), Atmospheric Modeling, Data Assimilation, and Predictability, 341

30   pp., Cambridge Univ. Press, New York

31   Key, J. R., D. Santek, C. S. Velden, N. Bormann, J.-N. Théopaut, L. P. Riishøjgaard, Y.

32   Zhu, and W. P. Menzel, 2003: Cloud-drift and water vapor winds in the polar regions

33   from MODIS. *IEEE Trans. Geosci. Remote Sens.,* **41,** 482–492.

34   Langland, R. H., and N. Baker, 2004: Estimation of observation impact using the NRL

35   atmospheric variational data assimila- tion adjoint system. Tellus, 56, 189–201.

36   Lazzara, M.A., R. ATCTorak, D.A. Santek, B.T. Hoover, C.S. Velden, and J.R. Key,

37   2014. High-Latitude Atmospheric Motion Vectors from Composite Satellite Data. *J.*

38   *Appl. Meteor. Clim*. 53, 534-547.

39   Marseille, G. J., A. Stoffelen, J. Barkmeijer, 2008. Sensitivity Observing System

40   Experiment (SOSE) - A New Effective NWP-based Tool in Designing the Global

41   Observing System. Tellus, A, 1, 60, 216-233, 10.1111/j.1600-0870.2007.00288.x

42   Mueller, K.J., M.J. Garay, C. Moroney, and V. Jovanovic, 2012: "Enhanced MISR Cloud

43   Motion Vectors: Performance Evaluation Relative to RAOB, MODIS, and GOES,"

44   11th International Winds Workshop, Auckland, New Zealand

Mueller, K.J., C.M. Moroney, V. Jovanovic, M.J. Garay, J-P Muller, L. Di Girolamo, and R. Davies, 2013a: MISR Level 2 Cloud Product Algorithm Theoretical Basis, JPL D-73327
http://eospso.gsfc.nasa.gov/sites/default/files/atbd/MISR_L2_CLOUD_ATBD-1.pdf

Mueller, K.J., C.M. Moroney, and V. Jovanovic, 2013b: "MISR Level 2 Cloud Product Quality Statement, September 14, 2012",
https://eosweb.larc.nasa.gov/sites/default/files/project/misr/quality_summaries/L2TC_Cloud_Product.pdf

Mueller, K.J., D.L. Wu, A. Horvath, V.M. Jovanovic, J.-P. Muller, L.D. DiGirolamo, M.J. Garay, D.J. Diner, C.M. Moroney, and S.Wanzong, 2017: Assessment of MISR Cloud Motion Vectors (CMVs) relative to GOES and MODIS Atmospheric Motion Vectors (AMVs). *J. Appl. Meteor. Climat*. doi:10.1175/JAMC-D-16-0112.1, in press.

Purser, R. J., W. Wu, D. F. Parrish, and N. M. Roberts, 2003a: Numerical aspects of the application of recursive filters to variational statistical analysis. Part I: Spatially homogeneous and isotropic Gaussian covariances. *Mon. Wea. Rev*., 131, 1524–1535.

Purser, R.J., W.-S. Wu, D.F. Parrish, and N.M. Roberts, 2003b: Numerical aspects of the application of recursive filters to variational statistical analysis. Part II: Spatially inhomogeneous and anisotropic general covariances. *Mon. Wea. Rev*., **131**, pp. 1536-1548.

Riishøjgaard, L.P., R. Atlas, and G. D. Emmitt, 2008: The Impact of ATCTL Observations on a Single-Level Meteorological Analysis. *J. Appl. Meteorol*. **44**, 1276–1277

67   Salonen, K., J. Cotton, N. Bormann, and M. Forsythe, 2015: Characterizing AMV

68   Height-Assignment Error by Comparing Best-Fit Pressure Statistics from the

69   Met Office and ECMWF Data Assimilation Systems. *J. Appl Climatol.*, 54, 225-242

70   Santek, D. 2010: The Impact of Satellite-Derived Polar Winds on Lower-Latitude

71   Forecasts. *Mon. Wea. Rev.*, **138**, 123–139

72   Stoffelen, A., G.J. Marseille, E. Andersson and D.G.H. Tan, 2005: Comments on The

73   Impact of Doppler Wind Observations on a Single-Level Meteorological Analysis

74   by L.P. Riishojgaard, R. Atlas and G.D. Emitt, J. Appl. Meteor., 44, 1276-1277.

75   Su, X., J. Derber, and J. Jung, 2012: Recent work on Satellite atmospheric motion

76   vectors in the NCEP data assimilation system. 11th International winds

77   workshop. February 20-24, 2012, Auckland, New Zealand

78   Wu, W.-S., R.J. Purser and D.F. Parrish, 2002: Three-dimensional variational analysis

79   with spatially inhomogeneous covariances. *Mon. Wea. Rev.*, **130**, 2905-2916.

80   Yamashita, K, (2014) The Impact of NASA TERRA MISR Atmospheric Motion Vector

81   Assimilation into JMAs Operational Global NWP System. *CAS/JSC WGNE Res.*

82   *Activ. Atmos. Oceanic Model*: http://www.wcrp-

83   climate.org/WGNE/BlueBook/2014/individual-

84   articles/01_Yamashita_Koji_WGNE_BB2014_MISR_yamashita_final.pdf

85   Zhu, Y., L. P. Riishojgaard, R. Davies, and C. Moroney, 2004: "Assessment and

86   application of MISR winds". 7th Int. Winds Workshop, Helsinki, Finland.

87   Zhu, Y. and R. Gelaro, 2008: Observation Sensitivity Calculations Using the Adjoint of

88   the Gridpoint Statistical Interpolation (GSI) Analysis System. *Mon. Wea. Rev.*,

89   **136**, 335–351. doi: http://dx.doi.org/10.1175/MWR3525.1

90

Figure Captions

Figure 1: Vertical profiles of per component forecast impact of UV, ATCT, and CT experiments

Vertical profiles for the southern hemisphere extra-tropics (left; a,d,g), the tropics (middle; b,e,h), and the northern hemisphere extra-tropics (right; c,f,i), are shown for sampling (top; a,b,c), observation minus 6-hour forecast (middle; d,e,f), and forecast impact (bottom; g,h,i) for the u and v components of MISR CMV in the UV experiment (labeled *uv u* and *uv v* in legend); the along-track (*ATCT at*) and cross-track (*ATCT ct*) in ATCT; and the cross-track components (*ct ct*) in CT.

Figure 2: Forecast impact of various observation types in ATCT and ATCT_15 experiments

The mean 24-hour forecast global (top; a,b) and a select regional (bottom; c,d) impact for selected types of observations in the ATCT_15 experiments as accumulated per 6-hours (left; a,c) and per observation (right; b,d). Error bars representing standard deviations are given, alongside percentages of total impact.

Figure 3: Mapped coverage of MISR CMVs relative to other classes of observation

Mapped coverage for five classes of observations assimilated in ATCT and ATCT_15 experiments spanning Sep.-Nov. 2014 and Mar.-May 2015. Coverage is measured per 2.5° latitude × 2.5° longitude map grid cell by the fraction of six-hour periods throughout experiments during which one or more observations were assimilated within that grid cell.

Figure 4: Adjoint forecast impact of MISR CMVs relative to other classes of observation.

As in Figure 2, but showing mean forecast impact accumulated per six-hour period in each map grid cell.

Figure 5: Time series of MISR CMV sampling and forecast impact per orbit for ATCT and ATCT_15

Time series of forecast impacts (top; a,b) and observation counts (bottom; c,d) for MISR CMV data during ATCT experiment (left; a,c) from Sep.-Nov. 2014 and ATCT_15 experiment (right; b,d) from Mar.-May 2015. Orbits with a net negative (i.e. beneficial) forecast impact are indicated in blue, the rest in red. Minima and maxima are shown in upper right. A running mean over 15 orbits (i.e. ~1 day) is plotted in black. Numbers of observations per orbit that were assimilated (blue) and rejected (red) are shown alongside a 15 orbit running mean (black).

Figure 6: Time series of MISR CMV sampling and forecast impact per orbit for NRT

As in Figure 5, but for experiment NRT.

134
135
136

7 Tables

Table 1 List of experiments, durations, and assimilation methods

| Experiment	Duration of experiment	MISR data product	Method of assimilating MISR winds
CONTROL	2014/09/02 - 2014/12/01	none	none
UV	2014/09/02 - 2014/12/01	MISR L3 CMV	joint u and v components
ATCT	2014/09/02 - 2014/12/01	MISR L3 CMV	independent along-track and cross-track components
CT	2014/09/02 - 2014/12/01	MISR L3 CMV	Only cross-track component
ATCT_15	2015/03/01 - 2015/06/01	MISR L3 CMV	independent along-track and cross-track components
ATCT_NRT	2014/09/02 - 2014/12/01	MISR NRT CMV	independent along-track and cross-track components

140

141 **Table 2 Overview of experiment statistics**

Label	MISR obs. per 6-hours	MISR obs. per valid orbit	MISR reject obs. per valid orbit	MISR impact per 6-hours ($J\ kg^{-1} \times 10^{-3}$)	MISR impact per valid orbit ($J\ kg^{-1} \times 10^{-3}$)	MISR impact per obs. ($J\ kg^{-1} \times 10^{-6}$)
UV	6000±3000	2400±360	520±160	-12±18	-4.8±10.4	-2.0±82.5
ATCT	6700±3100	2500±360	330±90	-25±18	-9.5±8.6	-3.7±78.8
CT	3300±1600	1300±180	170±40	-15±15	-5.9±8.3	-4.6±107.6
ATCT_15	8200±1900	2500±350	320±130	-27±17	-8.2±8.2	-3.3±79.5
ATCT_NRT	6000±2200	1900±600	240±120	-21±15	-6.8±7.6	-3.5±78.1

142

8 Figures

Figure 1: Vertical profiles of per component forecast impact of UV, ATCT, and CT experiments

Vertical profiles for the southern hemisphere extra-tropics (left; a,d,g), the tropics (middle; b,e,h), and the northern hemisphere extra-tropics (right; c,f,i), are shown for sampling (top; a,b,c), observation minus 6-hour forecast (middle; d,e,f), and forecast impact (bottom; g,h,i) for the u and v components of MISR CMV in the UV experiment (labeled *uv u* and *uv v* in legend); the along-track (*ATCT at*) and cross-track (*ATCT ct*) in ATCT; and the cross-track components (*ct ct*) in CT.
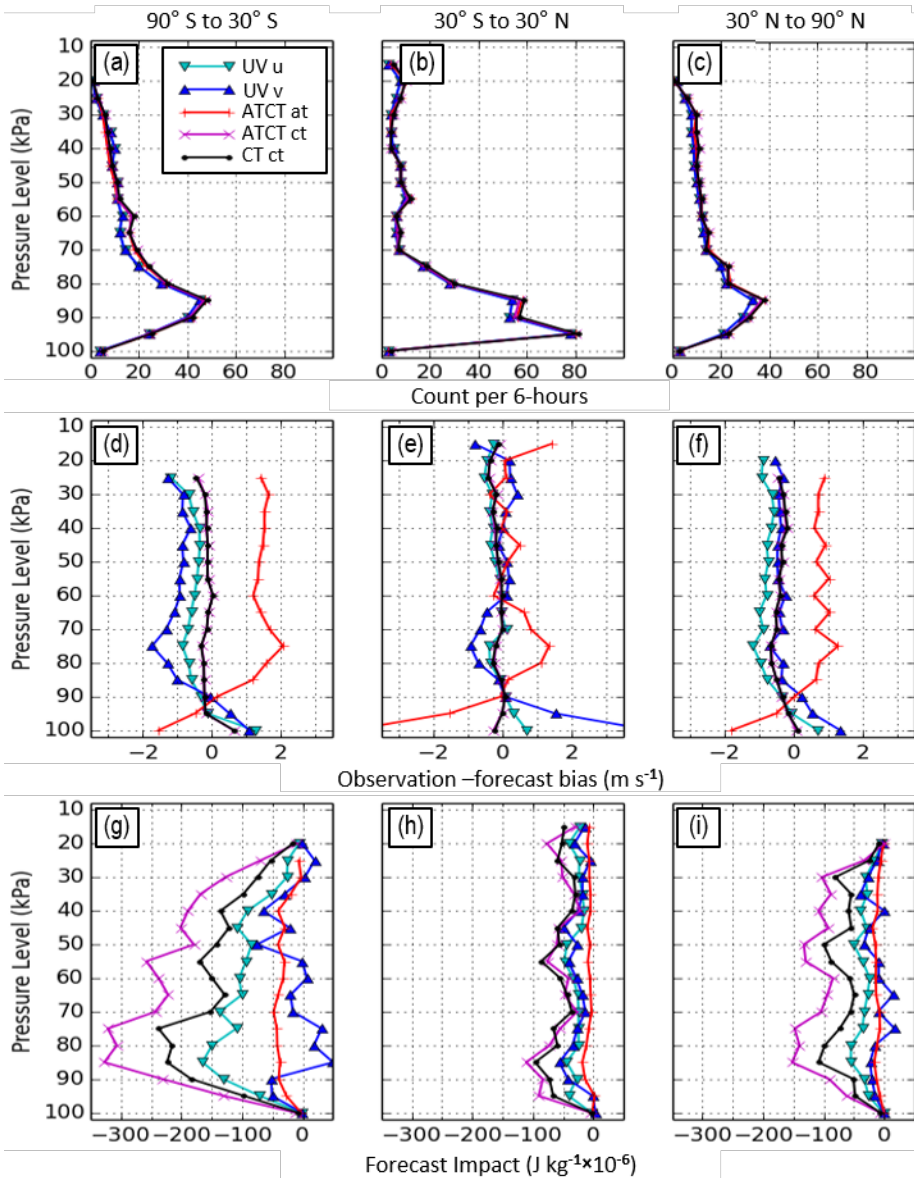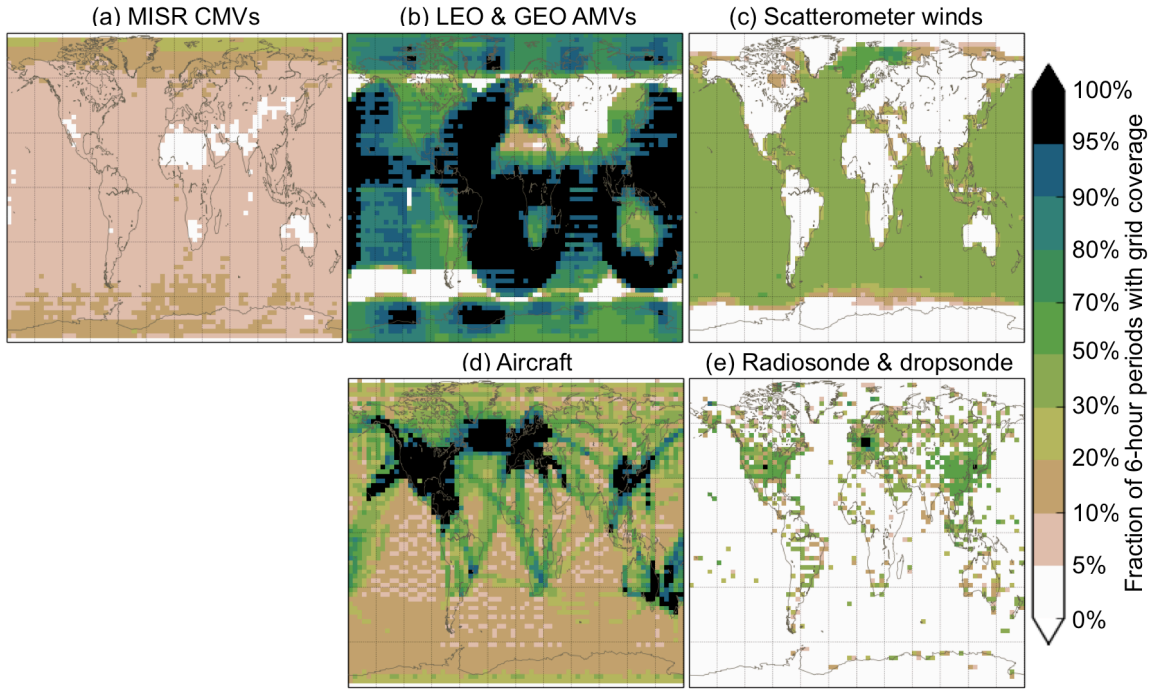
10   **Figure 2: Forecast impact of various observation types in ATCT and ATCT_15 experiments**

11   The mean 24-hour forecast global (top; a,b) and a select regional (bottom; c,d)
12   impact for selected types of observations in the ATCT_15 experiments as
13   accumulated per 6-hours (left; a,c) and per observation (right; b,d). Error bars
14   representing standard deviations are given, alongside percentages of total impact.
15

Global observation impact by type
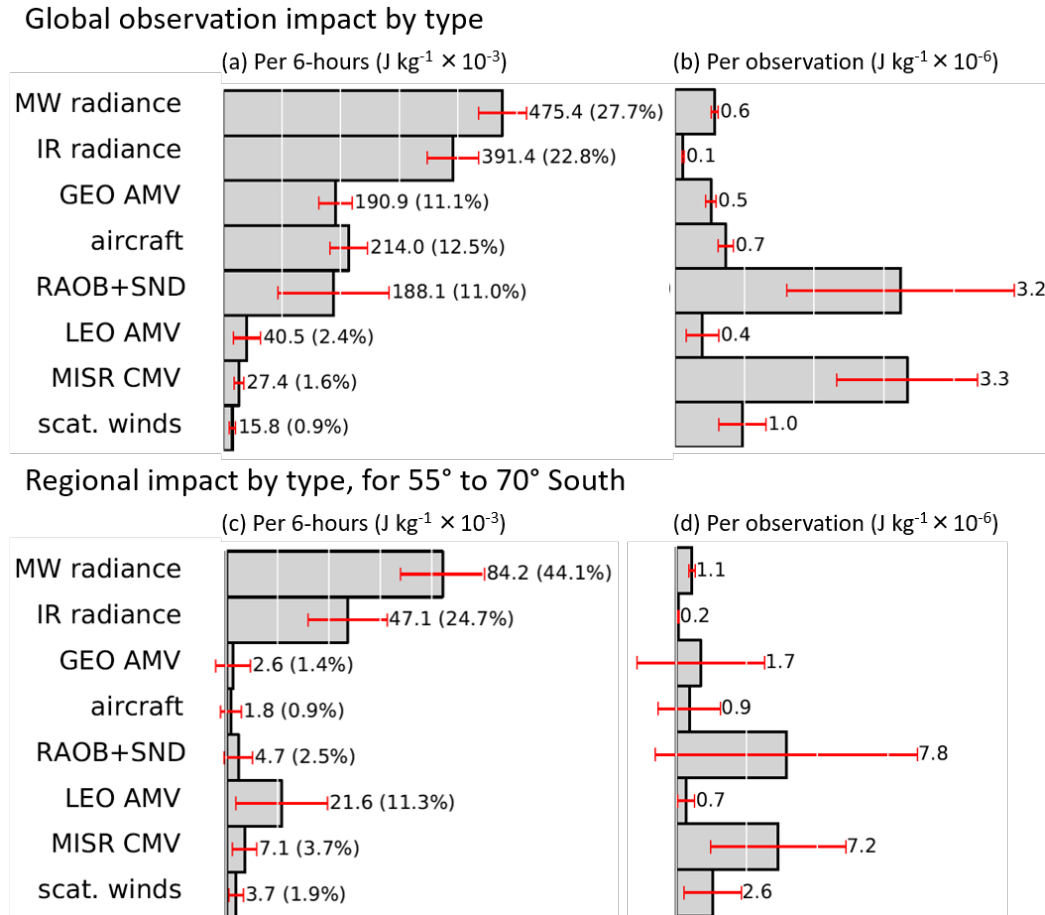
16
17   **Figure 3: Mapped coverage of MISR CMVs relative to other classes of observation**

18   Mapped coverage for five classes of observations assimilated in ATCT and ATCT_15
19   experiments spanning Sep.-Nov. 2014 and Mar.-May 2015. Coverage is measured
20   per 2.5° latitude × 2.5° longitude map grid cell by the fraction of six-hour periods
21   throughout experiments during which one or more observations were assimilated
22   within that grid cell.
23

(a) MISR CMVs   (b) LEO & GEO AMVs   (c) Scatterometer winds

(d) Aircraft   (e) Radiosonde & dropsonde

Fraction of 6-hour periods with grid coverage
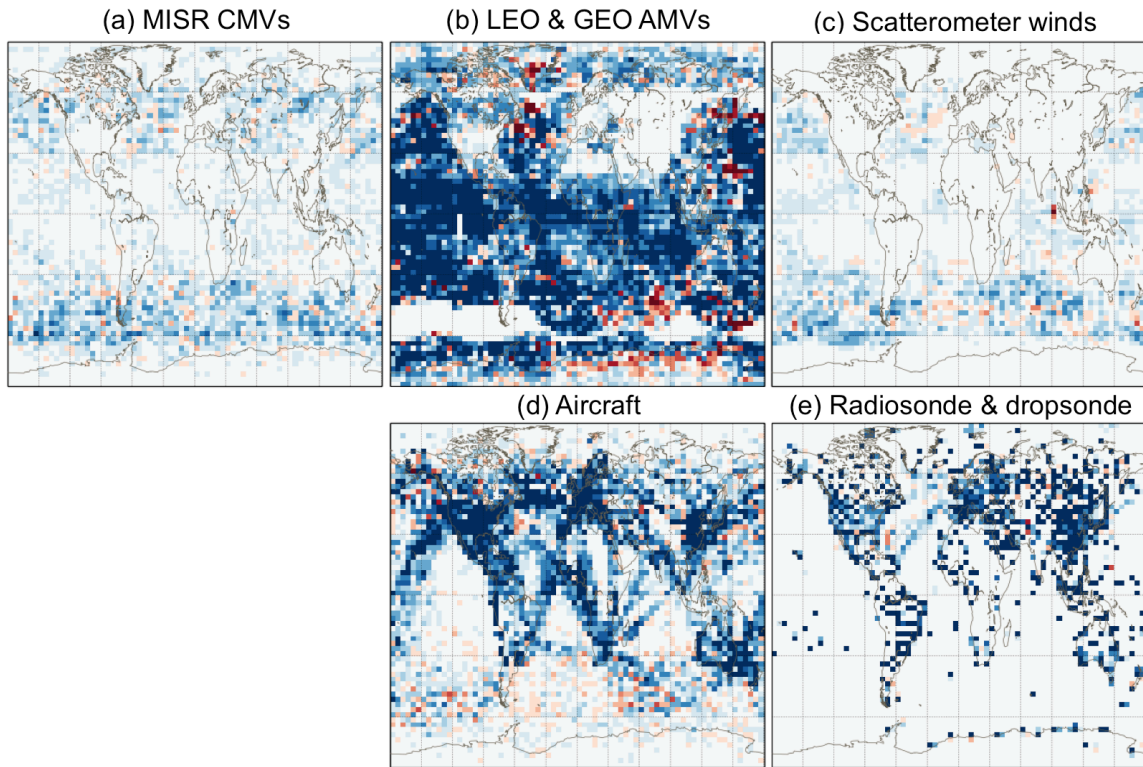
100%
95%
90%
80%
70%
50%
30%
20%
10%
5%
0%

24
25

26 **Figure 4: Adjoint forecast impact of MISR CMVs relative to other classes of observation.**

27 As in Figure 2, but showing mean forecast impact accumulated per six-hour period
28 in each map grid cell.
29

(a) MISR CMVs   (b) LEO & GEO AMVs   (c) Scatterometer winds

(d) Aircraft   (e) Radiosonde & dropsonde

30
31

32 **Figure 5: Time series of MISR CMV sampling and forecast impact per orbit for ATCT and ATCT_15**

33 Time series of forecast impacts (top; a,b) and observation counts (bottom; c,d) for
34 MISR CMV data during ATCT experiment (left; a,c) from Sep.-Nov. 2014 and
35 ATCT_15 experiment (right; b,d) from Mar.-May 2015. Orbits with a net negative
36 (i.e. beneficial) forecast impact are indicated in blue, the rest in red. Minima and
37 maxima are shown in upper right. A running mean over 15 orbits (i.e. ~1 day) is
38 plotted in black. Numbers of observations per orbit that were assimilated (blue)
39 and rejected (red) are shown alongside a 15 orbit running mean (black).
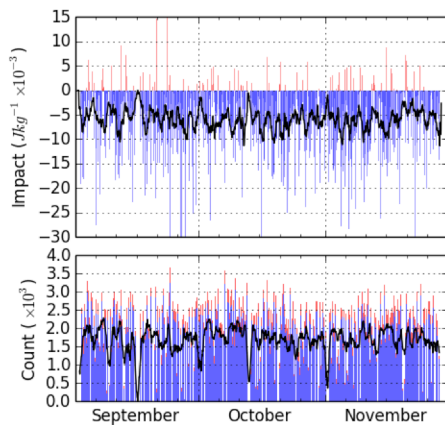40
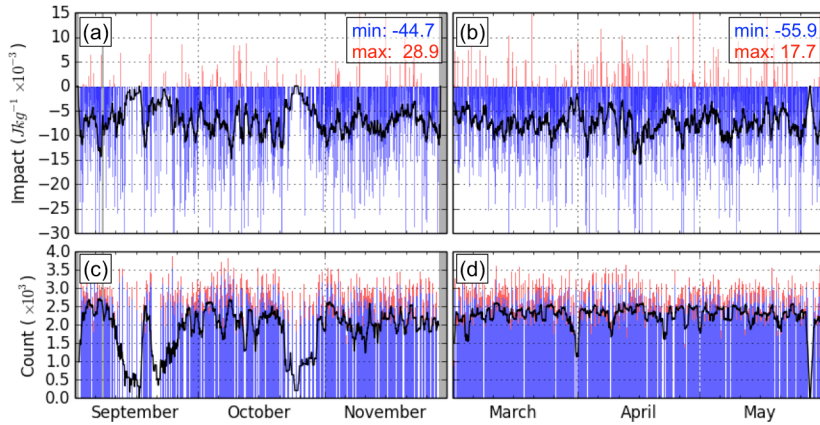
41
42
43 **Figure 6: Time series of MISR CMV sampling and forecast impact per orbit for NRT**

44 As in Figure 5, but for experiment NRT.

45
46